A high-angular-coverage optical diagnostic to measure scattered light directionality on Vulcan Target Area West

Contact: kevin.glize@stfc.ac.uk

K. Glize, X. Zhao, X.H. Yuan & J. Zhang
Key Laboratory for Laser Plasmas (MoE) and School of Physics and Astronomy, & Collaborative Innovation Center of IFSA, Shanghai Jiao Tong University, Shanghai 200240, China

Y.H. Zhang & Y.F. Dong
Beijing National Laboratory for Condensed Matter Physics, Institute of Physics, Chinese Academy of Sciences, Beijing 100190, China

Y.Y. Wang, B. Fisher, M. Khan & N.C. Woolsey
York Plasma Institute, University of York, York YO10 5DD, United Kingdom

E. Hume, G. Cristoforetti, P. Koester & L. Gizzi
Intense Laser Irradiation Laboratory, INO-CNR, 56124 Pisa, Italy

S. Zähter
Focused Energy GmbH, Im Tiefen See 45, 64293 Darmstadt, Germany

Abstract

We report on the design and implementation of a diagnostic with high angular coverage, measuring the spectrum and energy of the scattered light resolved in angle, both polar and azimuth. This diagnostic is fibre-based, and consists of a large structure holding 55 fibres at different angular positions, which are then bundled into a line and coupled to a fully calibrated imaging spectrometer. It is currently one of the only methods to provide information simultaneously on the scattering directionality and the total energy loss over a large solid angle arising chiefly from the stimulated Raman side-scattering, two plasmon decay, and cross beam energy transfer laser-plasma instabilties.

1 Introduction

Laser-plasma instabilities (LPI) [1] are still a critical issue in Inertial Confinement Fusion (ICF) experiments, limiting the achievable gain. In Direct-Drive schemes, such has central hot-spot [2], fast ignition [], shock ignition [3] or double-cone ignition [4], stimulated Raman scattering (SRS) is one of the most concerning LPIs, along with two-plasmon decay (TPD) and cross-beam energy transfer (CBET). The SRS mechanism leads to the scattering of a fraction of the incident laser, reducing the energy coupling, and generation of a hot electron population that can preheat the fuel core. A complex aspect of this instability is that it scatters light in multiple directions depending on the mechanism involved, namely, back-scattering, forward-scattering, and side-scattering. Recently, the predominance of the side-scattering geometry has been observed on several direct-drive experiments [5–8]. Stimulated Raman side-scattering (SRSS) is a particular SRS geometry in which the scattered light is initially emitted perpendicular to the density gradient. The proceeding scattered light directionality is then dictated by the refraction and thus the plasma profile, leading to a broad spectral emission over a very large soldi angle [8]. Due to the complexity of diagnosing SRSS on experiment, comprehensive measurements of this mechanism and related losses are still not available and further experimental characterisation is necessary.

To this end, a set of experiments were ini-

tially performed at the Shenguang-II Upgrade laser facility, fitting a newly developed diagnostic, designed specifically to measure the emission driven by SRSS, resolved in spectrum and energy: angularly-resolved scattered light diagnostic station or ARSDS [9]. However, this diagnostic collected the light scattered in a limited amount of directions, namely a single polar and and a single azimuthal plane. Furthermore, these measurement were obtained for an interaction with fixed parameters on a complex integrated experiment, limiting our understanding of the underlying SRSS physics and its impact on Direct-Drive schemes. An upgraded version of the ARSDS has been designed to be specifically implemented on Vulcan Target Area West (TAW) to measure the spectrum and energy of the scattered light over a broader angular domain: High Angular Coverage Side-scattering Station or HACSS. Such measurement enables the retrieval the spherical emission profile (θ, φ), and also provides an estimate of the total energy losses driven by SRSS. As a smaller scale facility TAW offers more freedom on the interaction design.

2 Experimental setup and related constraints

The diagnostic presented here was specifically designed to maximise the angular coverage while maintaining clear aperture for the incident laser beams. Therefore, a brief presentation of the experimental setup and the related geometrical constraints is required to understand the diagnostic design discussed in Section 3. For clarity, we define here that the target normal, along the z axis, is the origin $\theta = 0°$ of the polar axis, and the lower pole is the origin of the azimuth axis $\varphi = 0°$. The experiment involved five laser beams: four 1ω nanosecond beams and later a 2ω picosecond beam, focused on a planar target placed at the Target Chamber Center (TCC). The difference in frequency was set to minimise any parasitic signal from the long pulses that could overlap with the LPIs emission from the short pulse beam. The overall interaction setup

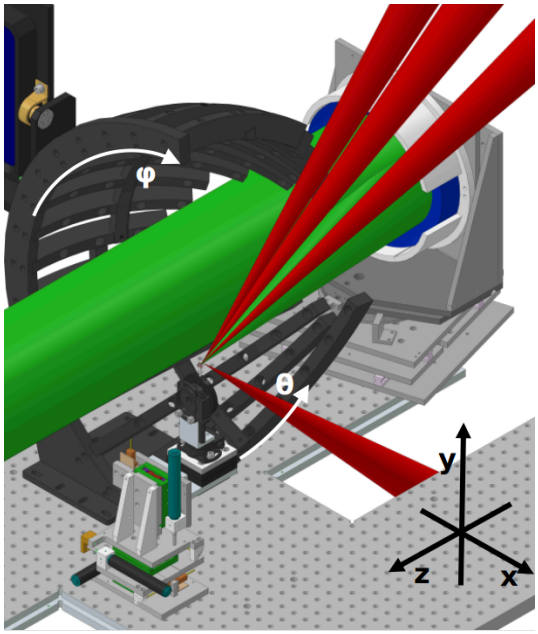

Figure 1: Layout of the experimental setup, with four plasma creation beams in red and the interaction beam in green. HACSS structure positioning and space limitation from beam geometry is clearly depicted. Cartesian and spherical coordinates are displayed for clarity.

is summarized on Fig. 1. The four long pulses irradiate the target with an $f/10$ aperture at angles $[\theta, \varphi] = [45°, 0°], [25°, 168°], [45°, 180°]$ and $[25°, 192°]$. Their purpose was to preform a plasma close to conditions anticipated in the direct-drive ICF regime. The short pulse was then used as the main interaction beam, to drive the LPIs of interest. It was focused onto the target by a $f/3$ off-axis parabola at the coordinate $[\theta, \varphi] = [15°, 90°]$, with a $s + 45°$ polarization (clockwise). Due to the focusing geometry, the 200 mm diameter collimated beam propagates close to the target which added more constraint on the available space for the diagnostic.

3 Diagnostic design

HACSS is a dedicated diagnostic which measures the light scattered from a laser-plasma interaction. The light is collected with a high angular coverage and propagated onto an imaging spectrometer in order to measure its spectrum

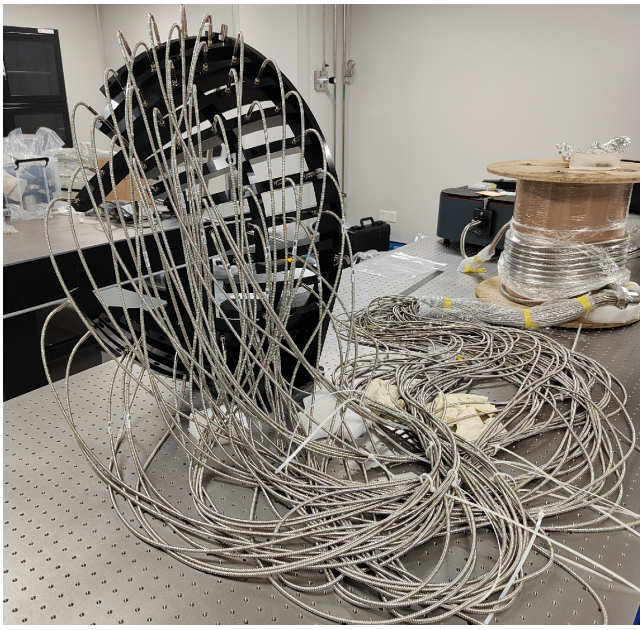

Figure 2: Actual HACSS structure holding the 55 fibres. Bundle and its connection to the spectrometer slit are visible at the back.

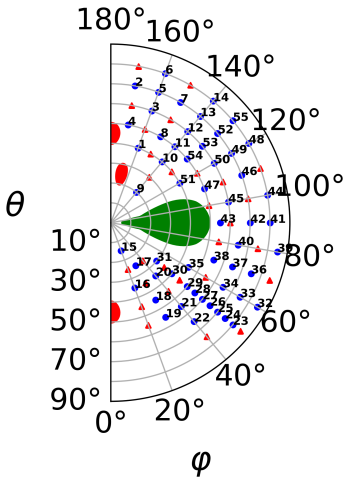

Figure 3: Spherical coordinate map of the available fibre port locations. Each blue circles was occupied by a fibre in the TAW experiment, and the red triangles are empty ports. The numbers correspond to the fibre position on the bundle. The beam areas are depicted by the red and green ellipses, representing the plasma creation and interaction beams, respectively.

and energy resolved in angle, and reconstruct the emission profile. The diagnostic consists of 55 fibres, mechanically held by an aluminium structure specifically designed to be compatible with the TAW experimental setup. The holding structure is displayed on Fig. 2, and consists of 16 arms, each covering a different azimuthal plane ranging from $\varphi = 20°$ to $\varphi = 170°$ with a $10° \pm 1°$ step. The structure's overall shape is a quarter of a sphere with a 400 mm radius centered at TCC. Precise alignment to TCC is realised by the use of two alignment stalks fitted on the structure, ensuring a pointing at TCC with a 3 mrad precision. Each arm has 0.5" threaded holes drilled every $10° \pm 1°$ along the polar axis θ which can accommodate SMA fibre adapter plates. Since stronger scattering is anticipated orthogonal to the laser polarisation direction based on previous experimental [10] and simulation results [11, 12], higher angular resolution of $5° \pm 1°$ steps was implemented on the $\varphi = 50°$ arm. The polar angle coverage is different for each arm, as these have been designed to cover as many angles as possible whilst maintaining clear aperture for the incident laser beams. In total, the structure provides 83 fibre ports at the locations indicated on Fig. 3, offering flexibility to easily modify fibre location during the experiment.

Fused silica step-index, VIS/NIR, stainless-steel jacket fibres with a numerical aperture = 0.22 and a 200 µm core diameter have been used. These fibres have a low attenuation in the spectral range of interest, namely $[600 - 900]$ nm. The 55 fibres were multiplexed into a single bundle through a vacuum feedthrough. The total length of each channel is 14m. The bundle was then imaged onto the slit of an Isoplane320 spectrometer. The incoming light was dispersed by a 150 g/mm, 500 nm blaze grating, and imaged onto an Andor NEO 5.5 Megapixel sCMOS camera. This enabled imaging the spectrum from the 55 fibres over a spectral range [570-840] nm and a resolution of ≈ 1.5 nm, avoiding any aberration on the edges as depicted on Fig. 4. A single ≤ 2 mm thick Schott glass Neutral Density filter (ND) ranging from ND.2 to ND.4 was placed at the entrance of the spectrometer to attenuate the signal.

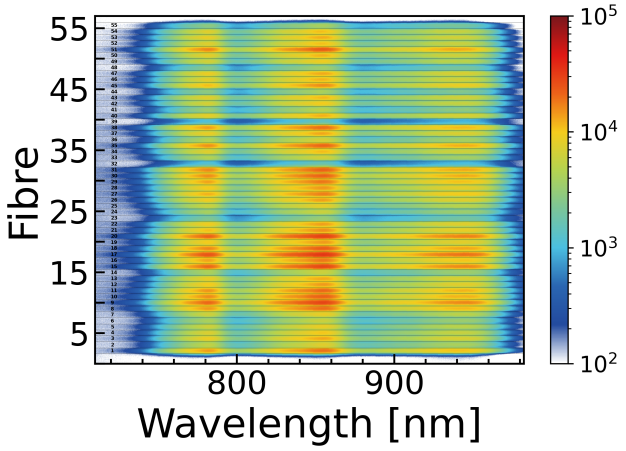

Figure 4: Spectra resolved in angle from the 55 fibres placed at the locations depicted on Fig. 3. The collected light was emitted from a NIR LED placed at TCC, and the acquisition duration was 100 ms. The grating was centered at 875 nm to image the whole spectrum from the LED source.

4 Energy calibration

Besides providing the scattered light spectrum resolved in angle, HACSS also provides a measurement of the amount of energy scattered against the angle. This requires an absolute calibration of the signal measured on the camera for each fibre. Two continuous LED sources of known spectrum were used to cover a spectral range from 500 to 1000 nm. Each LED source was placed, separately, at TCC, then the light power reaching each fibre was measured by a S120C photodiode power meter sensor. However, this sensor does not have a flat spectral response, so the power measured P_{meas} needs to be deconvolved from the sensor response $R(\lambda)$ to obtain the actual power at the fibre entrance. This is achieved using the following equation

$$P_{meas} = P_{max} \int Spec_{LED}(\lambda) \frac{R(\lambda)}{R(\lambda_{central})} d\lambda \quad (1)$$

where $Spec_{LED}(\lambda)$ is the normalised LED spectrum, P_{max} is the unknown power amplitude that is measured through this deconvolution, and $\lambda_{central}$ is the central wavelength value at which the power meter is used. The actual power at the fibre entrance is then calculated as

$$P_{actual} = P_{max} \int \frac{dP}{d\lambda} d\lambda \quad (2)$$

To obtain an energy calibration curve, several acquisitions are made on the camera, for different integration times τ. The energy entering the fibre for each acquisition can be expressed as

$$E = \tau \frac{\Omega_{fibre}}{\Omega_{meter}} P_{max} \int_{\lambda_1}^{\lambda_2} \frac{dP}{d\lambda} d\lambda \quad (3)$$

where Ω_{fibre} and Ω_{meter} are the solid angles of the the fibre and power meter sensor respectively, λ_1 and λ_2 are the wavelength limits imaged on the camera.

The next step is to measure the spectral transmission $T(\lambda)$ of the overall diagnostic which is easily obtained by dividing the spectrum on the camera $Spec(\lambda)$ by the known spectrum of the LED $Spec_{LED}$.

Last, the equations providing the response r of the diagnostic in J per count are

$$Signal_{[count]} = \int_{\lambda_1}^{\lambda_2} \frac{Spec(\lambda)}{T(\lambda)} d\lambda \quad (4)$$

$$r_{[J/count]} = \frac{E_{[J]}}{Signal_{[count]}} \quad (5)$$

This procedure was performed for all fibres, using the two LED sources covering visible and near-infrared spectrum, the latter being depicted on Fig. 4. The resulting calibration for three fibres is presented on Fig. 5.

5 Experimental measurement

The HACSS was implemented during a campaign at Vulcan TAW. Figure 6 shows a typical measurement obtained in a single shot during

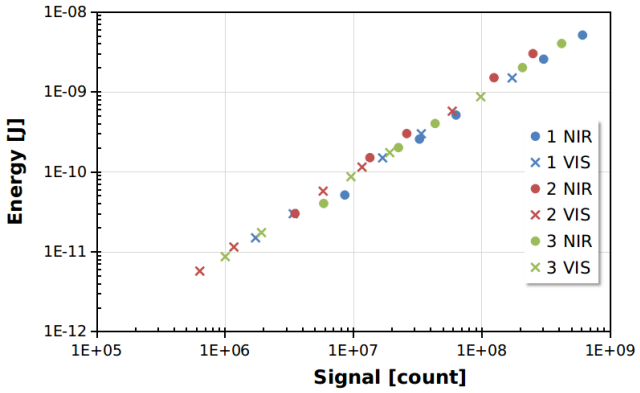

Figure 5: Calibration curve in energy against camera count for three fibres, obtained from two calibration sources, VIS and NIR LED.

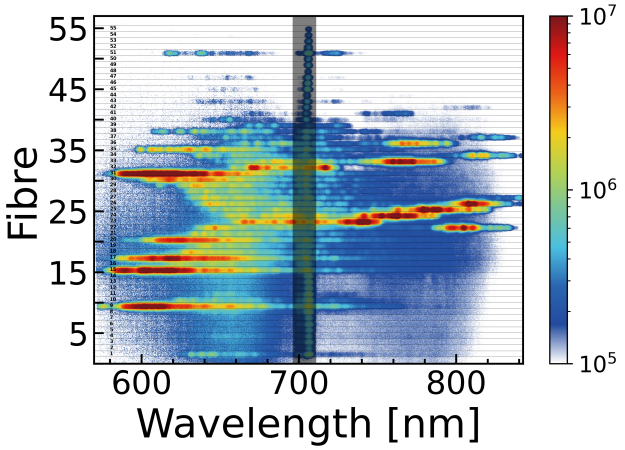

Figure 6: Example of spectra resolved in angle acquired during the experiment. It clearly displays the angular dependence of the spectrum for the emission driven by the interaction beam. The feature at 700 nm present at every angular position, and highlighted by a black shade, is driven by the plasma creation beams and is associated to the two-plasmon decay instability.

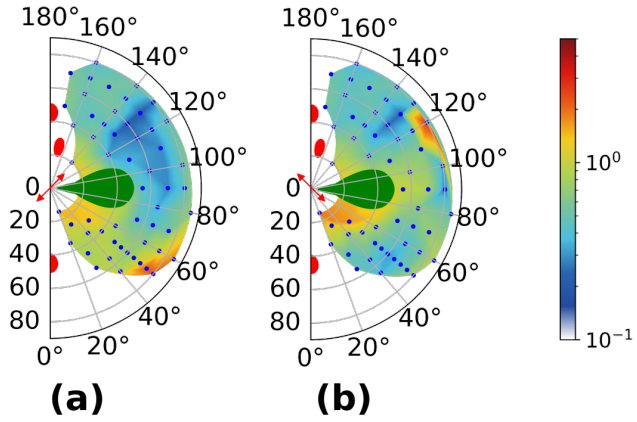

Figure 7: Emission profile in J/sr plotted in spherical coordinates, driven by a laser with (a) similar polarization as the spectra showed in Fig. 6 and (b) with an orthogonal polarization. The polarization orientation is indicated by the red arrow on both images.

the experimental campaign, with the fibres located at the positions depicted on Fig. 3. It shows the angular dependence of the spectrum, ranging from narrow- to broad-band depending on the angular position. These spectra are due to SRSS driven by the short pulse. An angularly independent signal is observed at 702 nm, highlighted in the black shade on Figure 6, corresponding to the $3\omega/2$ of the 1ω nanosecond heating beams. This feature is attributed to two plasmon decay and is a powerful diagnostic tool to measure the electron temperature of the plasma [13]. Hence, this diagnostic can provide not only valuable information on SRSS, but can also be used to aid characterisation of the plasma. By imaging a different spectral region, centered around 1ω with a higher dispersion grating, this diagnostic could also provide information on any CBET driven by the four nanosecond beams.

From the calibration in energy described in Section 4, the amount of energy scattered for each angle can be retrieved. An interpolated emission profile in spherical coordinates over π can be then be inferred, as presented on Fig. 7(a). As expected, a clear angular dependence on the scattering is present, with most of the

energy being scattered orthogonal to the laser polarization along the $\varphi = 50°$ arm. By rotating the polarization by 90° (*i.e.* $s - 45°$), it is possible to measure the emission profile over a different region with respect to the laser polarisation, as shown on Fig. 7(b). By combining the emission profile measured for both polarisation states, it is possible to extrapolate the scattering profile over $3\pi/2$ and estimate a total reflectivity from the SRSS instability. This is currently being developed and analysed.

6 Conclusion

We report here on the design and implementation of a dedicated diagnostic for the TAW facility, which was developed to study LPIs scattering light over a broad range of directions, namely SRSS but also TPD and possibly CBET. HACSS is a fibre based diagnostic offering collection over a π solid angle which measures the scattered light spectrum and energy resolved in angle, enabling a retrieval of the emission profile and an estimate of the total energy losses. This diagnostic, coupled with a carefully designed experimental setup, provides a powerful platform to study the complex emission profile of LPIs and improve our understanding of the underlying physics. The results will provide valuable information for any Direct-Drive approach to ICF, being the main direction considered for Inertial Fusion Energy facilities.

References

[1] W. L. Kruer. The Physics of Laser Plasma Interactions, W. L. Kruer. Addison-Wesley, 1988, £33.95, 182 pages. *Journal of Plasma Physics*, 45(1):135, January 1991. doi: 10.1017/S0022377800015555.

[2] John Lindl. Development of the indirect-drive approach to inertial confinement fusion and the target physics basis for ignition and gain. *Physics of Plasmas*, 2(11): 3933–4024, 1995. doi: 10.1063/1.871025.

[3] R. Betti, C. D. Zhou, K. S. Anderson, L. J. Perkins, W. Theobald, and A. A. Solodov. Shock ignition of thermonuclear fuel with high areal density. *Phys. Rev. Lett.*, 98:155001, Apr 2007. doi: 10.1103/PhysRevLett.98.155001.

[4] J. Zhang, W. M. Wang, X. H. Yang, D. Wu, Y. Y. Ma, J. L. Jiao, Z. Zhang, F. Y. Wu, X. H. Yuan, Y. T. Li, and J. Q. Zhu. Double-cone ignition scheme for inertial confinement fusion. *Philosophical Transactions of the Royal Society A: Mathematical, Physical and Engineering Sciences*, 378 (2184):20200015, 2020. doi: 10.1098/rsta.2020.0015.

[5] M. J. Rosenberg, A. A. Solodov, J. F. Myatt, W. Seka, P. Michel, M. Hohenberger, R. W. Short, R. Epstein, S. P. Regan, E. M. Campbell, T. Chapman, C. Goyon, J. E. Ralph, M. A. Barrios, J. D. Moody, and J. W. Bates. Origins and scaling of hot-electron preheat in ignition-scale direct-drive inertial confinement fusion experiments. *Phys. Rev. Lett.*, 120:055001, Jan 2018. doi: 10.1103/PhysRevLett.120.055001.

[6] M. J. Rosenberg, A. A. Solodov, W. Seka, R. K. Follett, J. F. Myatt, A. V. Maximov, C. Ren, S. Cao, P. Michel, M. Hohenberger, J. P. Palastro, C. Goyon, T. Chapman, J. E. Ralph, J. D. Moody, R. H. H. Scott, K. Glize, and S. P. Regan. Stimulated raman scattering mechanisms and scaling behavior in planar direct-drive experiments at the national ignition facility. *Physics of Plasmas*, 27(4):042705, 2020. doi: 10.1063/1.5139226.

[7] M. J. Rosenberg, A. A. Solodov, J. F. Myatt, S. Hironaka, J. Sivajeyan, R. K. Follett, T. Filkins, A. V. Maximov, C. Ren, S. Cao, P. Michel, M. S. Wei, J. P. Palastro, R. H. H. Scott, K. Glize, and S. P. Regan. Effect of overlapping laser beams and density scale length in laser-plasma instability experiments on omega ep. *Physics*

of Plasmas, 30(4):042710, 2023. doi: 10.1063/5.0135603. URL https://doi.org/10.1063/5.0135603.

[8] K. Glize, X. Zhao, Y. H. Zhang, C. W. Lian, S. Tan, F. Y. Wu, C. Z. Xiao, R. Yan, Z. Zhang, X. H. Yuan, and J. Zhang. Measurement of stimulated Raman side-scattering predominance in directly driven experiment. *Physics of Plasmas*, 30(12): 122706, 12 2023. ISSN 1070-664X. doi: 10.1063/5.0180607.

[9] X. Zhao, X. H. Yuan, J. Zheng, Y. F. Dong, K. Glize, Y. H. Zhang, Z. Zhang, and J. Zhang. An angular-resolved scattered-light diagnostic for laser-plasma instability studies. *Review of Scientific Instruments*, 93(5):053505, 2022. doi: 10.1063/5.0090841.

[10] R. P. Drake, R. E. Turner, B. F. Lasinski, K. G. Estabrook, E. M. Campbell, C. L. Wang, D. W. Phillion, E. A. Williams, and W. L. Kruer. Efficient raman sidescatter and hot-electron production in laser-plasma interaction experiments. *Phys. Rev. Lett.*, 53:1739–1742, Oct 1984. doi: 10.1103/PhysRevLett.53.1739.

[11] C. Z. Xiao, Z. J. Liu, C. Y. Zheng, and X. T. He. Competition between stimulated raman scattering and two-plasmon decay in inhomogeneous plasma. *Physics of Plasmas*, 23(2):022704, 2016. doi: 10.1063/1.4941969.

[12] C Z Xiao, H B Zhuo, Y Yin, Z J Liu, C Y Zheng, Y Zhao, and X T He. On the stimulated raman sidescattering in inhomogeneous plasmas: revisit of linear theory and three-dimensional particle-in-cell simulations. *Plasma Physics and Controlled Fusion*, 60(2):025020, jan 2018. doi: 10.1088/1361-6587/aa9b41.

[13] W. Seka, B. B. Afeyan, R. Boni, L. M. Goldman, R. W. Short, K. Tanaka, and T. W. Johnston. Diagnostic value of odd-integer half-harmonic emission from laser-produced plasmas. *The Physics of Fluids*, 28(8):2570–2579, 1985. doi: 10.1063/1.865265.